

Electrical readout of spins in the absence of spin blockade

Felix-Ekkehard von Horstig,^{1,2,*} Lorenzo Peri,^{1,3} Sylvain Barraud,⁴ Jason A. W. Robinson,² Monica Benito,⁵ Frederico Martins,⁶ and M. Fernando Gonzalez-Zalba^{1,†}

¹*Quantum Motion, 9 Sterling Way, London, N7 9HJ, United Kingdom*

²*Department of Materials Sciences and Metallurgy, University of Cambridge, Charles Babbage Rd, Cambridge CB3 0FS, United Kingdom*

³*Cavendish Laboratory, University of Cambridge,*

JJ Thomson Ave, Cambridge CB3 0HE, United Kingdom

⁴*CEA, LETI, Minatec Campus, F-38054 Grenoble, France*

⁵*Institute of Physics, University of Augsburg, 86159 Augsburg, Germany*

⁶*Hitachi Cambridge Laboratory, J.J. Thomson Avenue, CB3 0HE, United Kingdom*

(Dated: March 20, 2024)

In semiconductor nanostructures, spin blockade (SB) is the most scalable mechanism for electrical spin readout requiring only two bound spins for its implementation which, in conjunction with charge sensing techniques, has led to high-fidelity readout of spins in semiconductor-based quantum processors. However, various mechanisms may lift SB, such as strong spin-orbit coupling (SOC) or low-lying excited states, hence posing challenges to perform spin readout at scale and with high fidelity in such systems. Here, we present a method, based on the dependence of the two-spin system polarizability on energy detuning, to perform spin state readout even when SB lifting mechanisms are dominant. It leverages SB lifting as a resource to detect different spin measurement outcomes selectively and positively. We demonstrate the method using a hybrid system formed by a quantum dot (QD) and a Boron acceptor in a silicon p-type transistor and show spin selective and positive readout of different spin states under SB lifting conditions due to (i) SOC and (ii) low-lying orbital states in the QD. We further use the method to determine the detuning-dependent spin relaxation time of 0.1-8 μ s. Our method should help perform high-fidelity projective spin measurements in systems subject to strong SOC and may facilitate quantum tomography and state leakage studies.

Direct measurement of individual spins is an extremely challenging task given their small magnetic dipole moment. However, in semiconductor nanostructures, the charge dipole associated with electron tunneling can be sizable. Such divide in electronic properties is reflected in the vastly different state-of-the-art sensitivities for the spin (~ 10 spins/ $\sqrt{\text{Hz}}$ [1–3]) and charge degrees of freedom ($\sim 10^{-6}$ electrons/ $\sqrt{\text{Hz}}$ [4–6]) which has pushed researchers to develop spin-to-charge conversion techniques in conjunction with charge sensing for electrical spin readout. Energy filtering, for example, uses the difference in tunnel rates to a charge reservoir of Zeeman-split spins states confined to a quantum dot (QD) (or impurity) [7] whereas spin blockade (SB) uses quantum selection rules to inhibit tunneling between two-particle states with different spin numbers [8], see Fig. 1. In particular, SB is a more scalable mechanism for spin-to-charge conversion requiring only two bound spins for its implementation and has proven instrumental in achieving high fidelity readout of spin qubits [9–12] even at low magnetic fields [13] and high temperatures [14, 15].

Charge sensing, in conjunction with spin-to-charge conversion mechanisms as described above, relies partly on negative-result measurements. This means that only a specific subset of spin measurement outcomes may trigger the charge detector, while the absence of such trig-

ger may be attributed to the complementary subset [16]. However, this approach comes with drawbacks, including potential state leakage or spin-mapping errors [17]. Furthermore, various mechanisms may lift SB, such as strong spin-orbit coupling (SOC) – which allows two-particle states with different spin numbers to couple (Fig. 1b) [18, 19] – and low valley-orbit level splitting – allowing aligned spins to exist in different orbital or valley states of the same confining potential (Fig. 1c) [20, 21]. The former mechanism is particularly relevant to spins III-V materials [22–25] and novel spin qubit systems such as holes in germanium [26–29], and silicon QDs [30, 31] that have come at the forefront of semiconductor based quantum computing due their technical ease for spin manipulation via electric fields [32–36] and their potential for large scale integration [37, 38]. A key element in the operation of spin qubits in double QDs is rapid spin projection(separation) pulses through a singlet-triplet anticrossing which are utilized to read(initialize) the system [39]. However, the anisotropic nature of SOC on these systems results in magnetic field orientations in which SOC is strongly enhanced which may compromise satisfying the diabatic condition of the pulses and hence the ultimate achievable readout and initialization fidelity in scaled up systems.

To overcome these challenges, we present a methodology, based on dispersive readout techniques [40] and spin-to-charge conversion [41] that enables positive measurements of different spin states and that is suitable for spin state detection under SB lifting conditions. Our

* fer28@cam.ac.uk

† fernando@quantummotion.tech

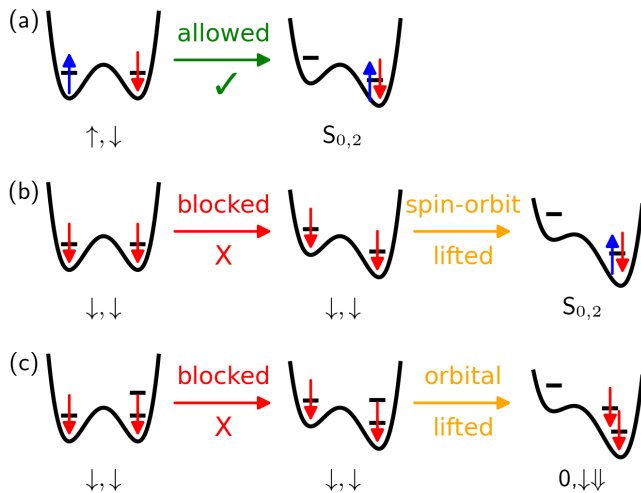


FIG. 1. Spin readout using spin-blockade: (a) Anti-aligned spins allow for the movement of spins, while (b,c) aligned spins are blocked, allowing for the two-particle spin states to be distinguished. SB can be lifted either by spin-orbit interaction (b) or by the presence of excited orbital states (c).

methodology makes use of energy-detuning dependence of the charge polarizability of the two-spin systems to positively detect either a spin parallel or an antiparallel measurement outcome without the need to perform a rapid diabatic pulse through a singlet-triplet anticrossing. The difference in polarizability manifest as a state-dependent quantum capacitance that can be detected through the dispersive interaction with a microwave superconducting resonator [42]. We demonstrate this readout methodology using a hybrid system subject to strong SOC formed by a hole QD and an acceptor in a silicon nanowire transistor and measure its spin relaxation time as a function of energy detuning. Finally, we expand the readout methodology to systems with low-lying orbital states, where SB may be lifted by allowed tunneling to the higher energy orbital. We implement the demonstration in a different charge configuration of our hybrid system, and show that the spin states can be mapped onto signals arising from the orbital ground and excited state charge transitions, allowing for the spin states to be measured selectively and positively.

I. SPIN BLOCKADE LIFTING VIA SPIN-ORBIT COUPLING

We use a p-type single-gate silicon transistor with light Boron channel doping, a system subject to strong SOC (Fig. 2a) [43]. By applying a voltage on the top-gate (V_g) and back-gate (V_{bg}), we accumulate holes in QDs formed in the nanowire, as well as in individual Boron atoms (Fig. 2b). We connect the gate of the transistor to a superconducting microwave (mw) resonator (panel a), to detect quantum capacitance changes arising from mw-

driven cyclic charge tunneling between the QD/Boron and the source and drain charge reservoirs (S,D) as well as between QDs and Boron atoms. We refer to the latter as interdot charge transitions (ICTs).

We tune the device to an ICT between a Boron atom and a QD (ICT A) with nominal charge occupation of $(N_B, N_D) = (1,1)/(2,0)$ (Fig. 2c) and a gate lever arm asymmetry $\Delta\alpha = 0.26 \pm 0.03$, a parameter used to convert gate voltage to energy detuning between the QD and Boron atom, see App. A for the full charge stability map. Throughout this work, we provide state occupations in the form (B,D), where the first will refer to the state of the Boron atom and the second to that of the QD. To characterise the spin eigenstates of the system, we perform magneto-spectroscopy [44] by measuring the resonator response against gate voltage across the ICT and magnetic field strength applied in the plane of the sample (Fig. 2d). The data reveals an enhancement of the resonator response which shifts up in V_g as the magnetic field is increased above $B \approx 0.2$ T. This is the signature of an effective two-spin system subject to strong SOC where, above 0.2 T, the system is free to tunnel between the polarised triplet state $(\downarrow_B, \downarrow_D)$ and the joint singlet $(S_{2,0})$ [45]. This is SOC-mediated spin blockade lifting which we describe in detail below.

We consider the two-particle SOC Hamiltonian in App. B that takes into account the g -factor of the Boron(QD) $g_{B(D)}$ (where in our case $g_B < g_D$) and the spin-conserving and spin-flip tunnel coupling, Δ_{sc} and Δ_{sf} . In Fig. 2e, we plot the simulated magneto-spectroscopy, as well as the eigenenergies and capacitive signals (Fig. 2 f,h and g,i) arising from the lowest two states at $B = 0(1)$ T. For $B < 0.2$ T, the capacitive signal arises from charge tunneling between the ground $(\uparrow_B, \downarrow_D)$ and $S_{2,0}$ states, mediated by the finite Δ_{sc} , see blue traces in panel g. For $B > 0.2$ T, however, the signal arises from the tunneling between the Zeeman split $T_{1,1}^- = (\downarrow_B, \downarrow_D)$ and the $S_{2,0}$ state, in this case mediated by Δ_{sf} , see the red traces in panels g and i. The good match between the experiment and simulations confirms the presence of the lifting mechanism since, for systems with low SOC, like few-electron QDs in silicon, such spin-flip tunneling processes are forbidden resulting in the signal vanishing asymmetrically at high fields (see the simulation in the insert of Fig. 2e) [46].

Magneto-spectroscopy allows us to quantify the parameters in the Hamiltonian. First, we obtain the average g -factor of the hole spin in the QD and Boron, $\bar{g} \sim 2$, which is given by the slope of the transition in the $T_{1,1}^-/S_{2,0}$ regime ($\bar{g} = e\alpha\Delta V_g/\mu_B B$), where e is the electron charge and μ_B the Bohr magneton [47]. Further, from the linewidth of the signal at zero and high field ($T_{1,1}^-/S_{2,0}$ regime), we extract the total charge and spin-flip coupling rates, $\sqrt{2}\Delta_c = \sqrt{\Delta_{sc}^2 + \Delta_{sf}^2} \sim 10.4$ GHz and $\Delta_{sf} \sim 3.4$ GHz, respectively. Additionally, by measuring the shift in V_g of the Boron-reservoir transition with magnetic field (not shown), we find the g -factor of the Boron $g_B \sim 1.6$ making the g -factor of the QD, $g_D \sim 2.4$.

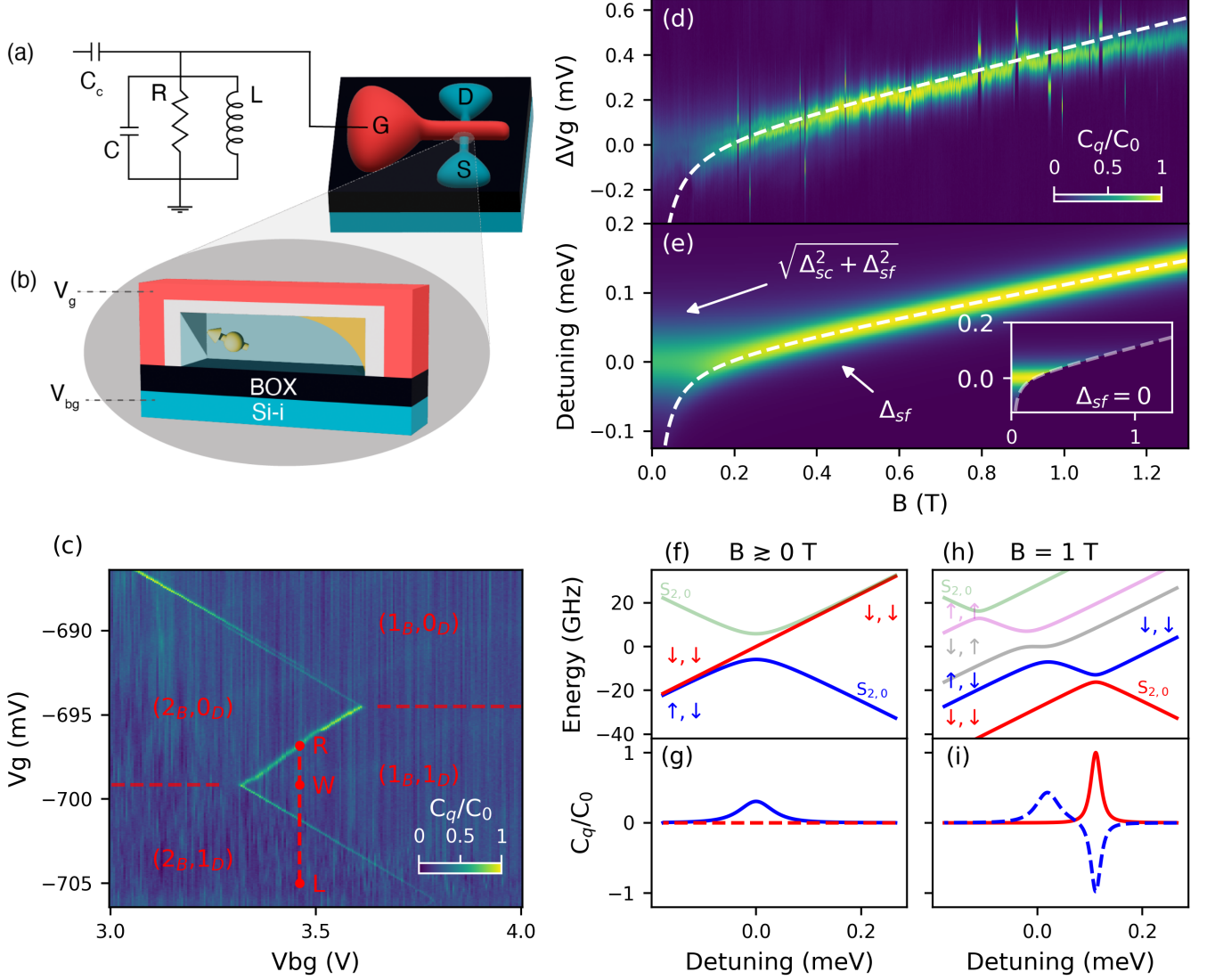


FIG. 2. Device description and readout concept: (a) Schematic of silicon nanowire transistor (top-view), labelled with Source (S), Drain (D) and top-gate (G) contacts, embedded in an LCR resonator for charge readout. (b) Schematic side-view of Si-nanowire with gate stack including gate metal (red), gate oxide (grey), channel (transparent blue), buried oxide (BOX in black) and intrinsic silicon substrate (Si-i, also blue). The corner QD and Boron atom where holes are confined are marked in yellow. (c) Charge stability diagram showing the capacitive signal measured in the V_g - V_{bg} space near the boron-dot transition (positive slope). A boron-reservoir transition is also visible (negative slope). The charge occupation are annotated in the plot. The approximate location of the dot-reservoir transition is indicated in red dashed lines. Location of Load, Wait and Read voltages for readout measurements are marked in red. (d) Magneto-spectroscopy measurement near the point labelled R in the stability diagram. The dotted line shows the location of the $T_{1,1}^-/S_{2,0}$ anticrossing. (e) Simulated magneto-spectroscopy of the same transition. The insert shows a simulation of the same transition with $\Delta_{sf}=0$, showing the emergence of SB. (f,h) Energy level diagram at two magnetic fields. (g,i) Capacitive signal of the lowest two states (\uparrow_B, \downarrow_D) and ($\downarrow_B, \downarrow_D$) at two magnetic fields. In each case the excited state is plotted in dashed lines.

II. SPIN READOUT UNDER SPIN-ORBIT LIFTED SB

Spin blockade is based on the exclusion principle in which two fermionic particles cannot possess all the same quantum numbers. It is utilized in DQDs to project the

combined spin state of two separated spin carrying particles into that of a single QD whose ground state is the joint singlet, $S_{2,0}$. Particularly, the polarized Triplets $T_{1,1}^\pm$ are blocked from transitioning into $S_{2,0}$ a feature that is used for spin parity readout, or for Pauli spin blockade if the unpolarized triplet state T^0 is also

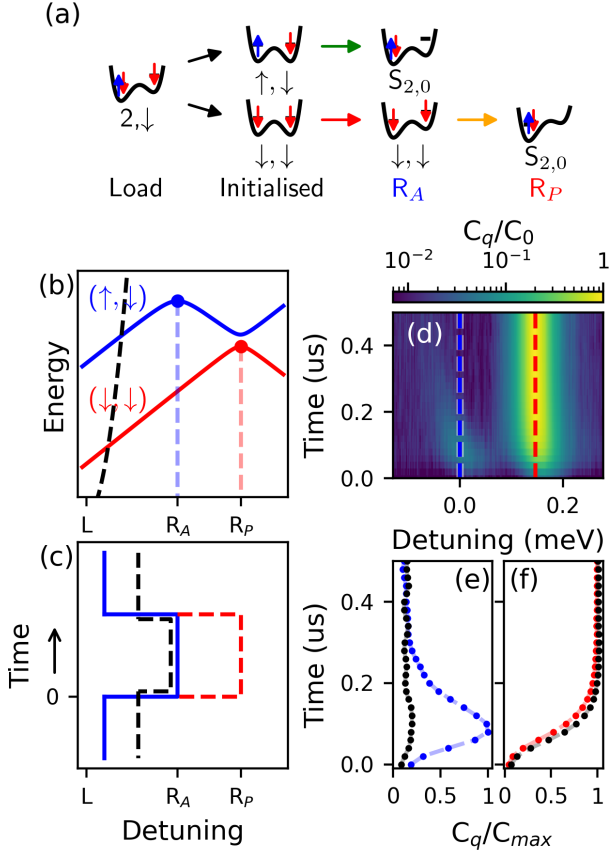


FIG. 3. Readout protocol with spin-orbit coupling: (a) Schematic of pulsing scheme. The state is initialised by randomly unloading a spin from the Boron atom starting from a $(2, \downarrow)$ configuration resulting in either a $(\downarrow_B, \downarrow_D)$, or a $(\uparrow_B, \downarrow_D)$. The measurement is performed either at R_A [triggered by the $(\uparrow_B, \downarrow_D)$ state] or at R_P [triggered by the $(\downarrow_B, \downarrow_D)$ state]. (b) Energy level diagram showing the load (L) and read points for the two states (R_A , R_P). The black dashed line denotes the Boron-reservoir transition between the $(2,1)$ and the $(1,1)$ charge states. (c) Schematic of pulse sequence for spin readout. States are initialised at L, and then pulsed to either R_A or R_P (blue or red lines). The black dashed lines indicates the control pulse where the state is initialised in the $(1,1)$ region. The time at which data acquisition is started is indicated. (d) Capacitive signal as a function of measurement time and detuning showing two signals arising from the $(\downarrow_B, \downarrow_D)$ and $(\uparrow_B, \downarrow_D)$ states. R_A and R_P are indicated with dashed lines. Measurements carried out at $B = 1$ T. (e, f) Line-cuts of d at detuning of R_A and R_P showing the capacitive signal (normalised to the peak value of each trace) against time. Dashed lines are given as a guide to the eye. The black lines are the signals recorded from the control measurement.

blocked [48]. In the presence of SOC, however, Δ_{sf} enables tunnelling of the $T_{1,1}^{\pm}$ states into the $S_{2,0}$, eliminating the spin selectivity of SB readout via projective measurements unless a fast diabatic pulse across the Δ_{sf} anticrossing can be performed. Such a requirement that may be challenging in practice if Δ_{sf} is large, ultimately limiting the fidelity of the spin-to-charge conversion mechanism (See App. C).

In this work, we use Δ_{sf} to our advantage. The finite spin flip coupling term between the $T_{1,1}^-$ and $S_{2,0}$ spin branches generates a distinct anticrossing at positive energy detuning ε . Most critically, for the purpose of our demonstration, we note that the capacitive signals arising from the anticrossings of the aligned $(\downarrow_B, \downarrow_D)$ and anti-aligned $(\uparrow_B, \downarrow_D)$ spin outcomes occur at different detuning (see the red and blue traces in Fig. 2i respectively) a concept that we exploit in the following for spin readout. We note that, additionally, the $T_{1,1}^+ = (\uparrow_B, \uparrow_D)$ and $S_{0,2}$ states anticross at a third readout point at negative detuning (see Fig. 2h), allowing for the $T_{1,1}^+$ population to be distinctly measured. We discuss this concept further in the App. D 1.

To measure the spin of the Boron, we first randomly initialise the system in either $(\uparrow_B, \downarrow_D)$ or $T_{1,1}^-$. We do so by starting in the $(2_B, 1_D)$ charge state (point L in Fig. 2c) to then pulse into the $(1_B, 1_D)$ region (point W), which randomly unloads a spin from the Boron atom, as illustrated in Fig. 3a. We then pulse to either of the readout points (R_A , R_P) and measure the dispersive signal in the time domain, see Fig. 3d-f. For these preliminary experiments, we set the wait time at W to $t_W = 0$ s. Additionally, we perform a control measurement in which we wait in the $(1,1)$ region to deterministically initialize the system in the $T_{1,1}^-$ by relaxation (see pulse sequences in Fig. 3c and Methods).

We observe two signals at different detuning (panel d), the separation of which depends on the magnetic field intensity as anticipated (see App. E). When we take a cut at zero detuning (panel e), we observe the signal from the $(\uparrow_B, \downarrow_D)$ - $S_{2,0}$ anticrossing, i.e. a $(\uparrow_B, \downarrow_D)$ measurement outcome. The signal initially rises, due to the finite ring up of the resonator, before decaying with a time constant $T_1 \sim 100$ ns given by the relaxation time to the T^- state (blue trace). At finite positive detuning (R_P), on the other hand, we observe signals arising from the $T_{1,1}^-$ - $S_{2,0}$ anticrossing, i.e. a $T_{1,1}^-$ measurement outcome (Fig. 3f). In this case, the signal (red trace) is delayed with respect to the resonator ring up (black trace). The slower dynamics is caused by the fraction of $(\uparrow_B, \downarrow_D)$ shots that carry a negative quantum capacitance at R_P , hence reducing the signal at timescales comparable to the relaxation time of 95 ns in this case. Our result shows that, in spin systems with lifted SB due to SOC, the spin state can be read using the different detuning points at which the dispersive signal of the $(\uparrow_B, \downarrow_D)$ and $T_{1,1}^-$ measurement outcomes manifest. This measurement is done without the need to perform a perfectly diabatic pulse through the $T_{1,1}^-$ - $S_{2,0}$ anticrossing.

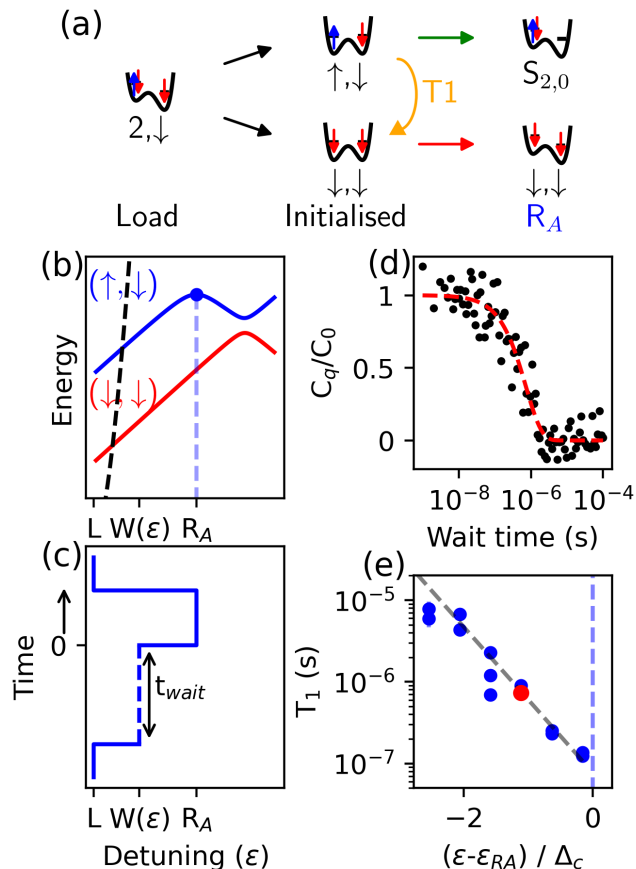


FIG. 4. T_1 characterisation: Measurements carried out at $B = 700$ mT. (a-c) Schematic of the measurement protocol: The state is initialised as described in Fig. 3. This is followed by a Wait ($W(\epsilon)$) period of variable time and pulse depth in which (\uparrow_B, \downarrow_D) may relax into $T_{1,1}^-$. Finally the state is read out at the spin anti-parallel readout point (R_A). The location of $W(\epsilon)$ is varied to characterise T_1 as a function of ϵ . The time at which data acquisition is started is indicated. (d) Example capacitive signal [a proxy for the (\uparrow_B, \downarrow_D) population] against t_w at $\epsilon = -92 \mu\text{eV} = -1.12 \Delta_c$ (red dot panel e). The data is taken from the maximum signal of line traces similar to that in Fig. 3d. The data is fitted using an exponential decay to extract T_1 (730 ± 80 ns in this case). (e) T_1 against detuning of the wait location $W(\epsilon)$ showing an exponential dependence (black dashed line) with detuning. The location of R_A is marked in blue. The data in panel d is marked with a red dot.

III. SPIN RELAXATION TIME

To demonstrate the benefit of this spin readout mechanism, we now study the spin qubit decay constant T_1 as a function of detuning. We again initialise randomly in the (\uparrow_B, \downarrow_D) or $T_{1,1}^-$ state but wait in the (1,1) region (point $W(\epsilon)$) for a variable time before pulsing to the readout point R_A (Fig. 4a-c). For long t_w , the initialised state will have a higher chance to decay to the ground state resulting in a reduction in the average excited state signal

(Fig. 4d). We extract T_1 by fitting the data to an exponential decay of the form $P_S(t_w) \propto \exp(-t_w/T_1)$ (red dashed line). We repeat this measurement for different detuning points and find that T_1 increases exponentially away from the readout point (Fig. 4e) up to $8 \mu\text{s}$, increasing its utility as a spin qubit.

IV. SPIN READOUT UNDER ORBITALLY LIFTED SB

In projective SB measurements, the presence of low-lying excited orbital or valley states (of energy δ_o) lifts SB by allowing spin triplets ($T_{0,2}$) to exist in the (0,2) charge configuration. Hence, when the energy detuning exceeds δ_o , both triplet and singlet are allowed to transition into the (0,2), eliminating spin selectivity of the charge movement (Fig. 1c). This mechanism limits the magnetic fields at which SB can be performed in transport measurements to $B < \delta_o/(\bar{g}\mu_B)$ [20] and limits the size of the voltage window in which SB can be detected in charge sensing experiments [49].

The presence of the orbital state results in a distinct anticrossing between the $T_{1,1}$ to $T_{0,2}$ states [21], separated in detuning from the spin anti-parallel anticrossing by δ_o (at zero magnetic field) as shown in Fig. 5d. These anticrossings result in two separate readout points corresponding to the spin anti-parallel and triplet outcomes (Fig. 5e,g). In this section, we demonstrate that the readout mechanism described in the context of SOC, naturally extends to anticrossings arising from orbital states, in this case by measuring the spin state of the hybrid DQD at two distinct detuning points. Such approach allows to selectively and positively detect different spin measurement outcomes.

For the demonstration, we tune the device to a different ICT comprising a different Boron atom and QD (ICT B) with nominal charge occupation $(N_B, N_D) = (1,1)/(0,2)$ and differential lever arm $\Delta\alpha = 0.54 \pm 0.02$ (Fig. 5a). Notably, in the (0,2) configuration the two holes reside within the QD, in contrast to ICT A where they resided in the Boron. The presence of low-energy orbital excited states in the QD allow for an orbital lifting of SB. We perform magneto-spectroscopy and again find an enhancement of the signal at magnetic fields above 300 mT characteristic of a two-spin-system with SOC. However, in this case, we additionally find that above 600 mT the signal remains at a fixed V_g point and its intensity is reduced, the signature the $T_{1,1}^-$ to $T_{0,2}^-$ transition is now allowed [21].

From magnetospectroscopy (Fig. 5b), we extract $\Delta_c \sim 20$ GHz, $\Delta_{\text{sf}} \sim 4$ GHz, $\delta_o \sim 20$ GHz, where δ_o is the QD excited state energy. From the slope of the transition in the $T_{1,1}^-/S_{0,2}$ and the $T_{0,2}^-$ regimes, we extract the average g -factor, $\bar{g} = 2.1 \pm 0.1$, and g -factor difference $\delta g = g_B - g_D = 0.3 \pm 0.1$, respectively. We extend the Hamiltonian to include the $T_{0,2}^-$ state (App. B) and simulate the magnetospectroscopy in Fig. 5c. In the

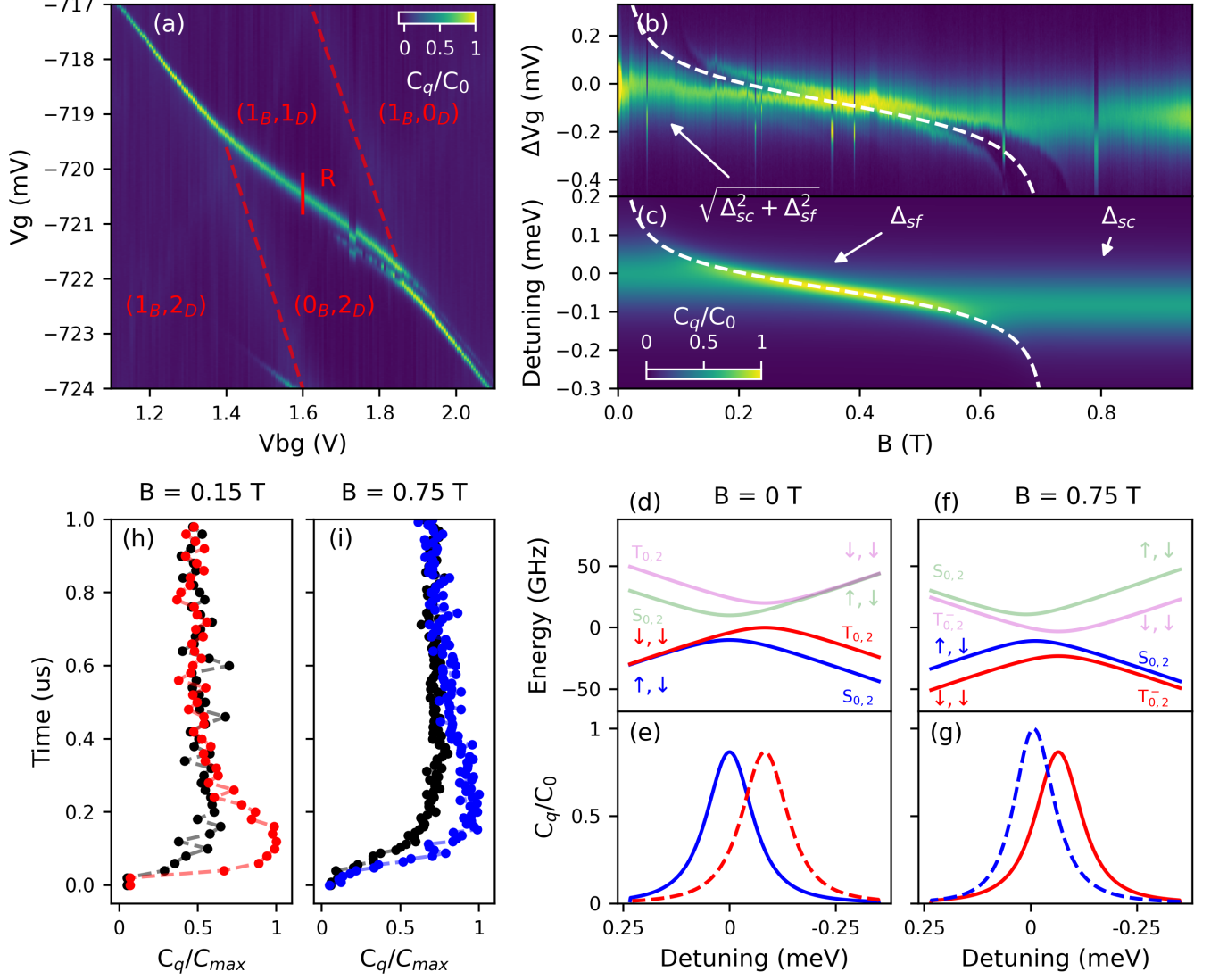


FIG. 5. Readout utilising orbital states: (a) Stability diagram of ICT B showing the nominal charge occupation. The readout location is highlighted. (b,c) Magneto-spectroscopy and simulation at the point marked R in a. (d,f) Energy level diagrams showing the energy levels of the transition at two magnetic fields. (e,g) Capacitive signals from the $(\uparrow_B, \downarrow_D)/S_{0,2}$ (blue) and $T_{1,1}^-/T_{0,2}^-$ (red) anticrossings marking the two readout locations. In each case the excited state is marked in dashed lines. (h,i) Capacitive signal measured, used to distinguish $(\uparrow_B, \downarrow_D)$ and $T_{1,1}^-$ states utilising the orbital $T_{1,1}^-/T_{0,2}^-$ transition (low magnetic field) or the $(\uparrow_B, \downarrow_D)/S_{0,2}$ transition (high magnetic field) as readout points. The response is normalised to the maximum of each linetrace.

data, we note the additional edges in the signal parallel to the $T_{1,1}^-/S_{0,2}$ anticrossing (white dashed line), see Fig. 5b. These arise due to resonant interactions between the spin system and photons in the mw resonator (2.1 GHz). Although less clear, these can also be observed in Fig. 2d.

We plot the energy-level diagrams and capacitance from the ground and first excited states at $B = 0$ T and $B = 0.75$ T in Fig. 5d-g. For ease of readability, we only include the $T_{1,1}^-$ and $(\uparrow_B, \downarrow_D)$ states in the (1,1) charge region and the $T_{0,2}^-$ in the (0,2) region. We further set

$\Delta_{sf} = 0$, since it is less relevant at fields explored in this section, i.e. outside the intermediate field regime where the T^-/S anticrossing occurs. At magnetic fields below and above the T^-/S regime, two distinct readout points emerge corresponding to the $(\uparrow_B, \downarrow_D)/S_{0,2}$ anticrossing (ground state at low magnetic field), and the $T_{1,1}^-/T_{0,2}^-$ anticrossing (ground state at high magnetic fields), separated in detuning by $\delta_o + ([g_B - g_D^*]/2)\mu_B B$, where g_D^* is the g -factor of the excited state of the doubly occupied QD.

We now demonstrate readout in each of these regimes.

First, at low field ($B = 0.15$ T), we use the $T_{1,1}^-/T_{0,2}^-$ anticrossing as the readout point. We start deep in the (1,1) region, where the ground state is $T_{1,1}^-$, to then perform a diabatic passage through the $T_{1,1}^-/S_{0,2}$ anticrossing to prepare the system in the excited $T_{1,1}^-$ state near zero detuning. Finally, we ramp to the $T_{1,1}^-/T_{0,2}^-$ anticrossing and gather the time-domain response (red points in Fig. 5h). We observe an initial resonator ring-up followed by a decay with $T_1 \sim 140 \pm 50$ ns (see Methods). In this case, the signal does not fully decay to zero as it was the case for the SOC experiments. This is a particularity of our concrete experiments since the signal from the ground state can also be detected at the readout point since $\delta_o \lesssim \Delta_{sf}$ (note the overlap in the C_q peaks in Fig. 5e and g). We discuss this limitation further in App. F. We compare the signal to a control measurement where we initialise in the ground state deep in the (0,2) region by waiting for relaxation to the $S_{0,2}$ state. We then ramp to the readout point (black points). In this case, the system remains in the ground state and the signal rises with the ring up of the resonator.

For the high field case ($B=0.75$ T), where we use the $(\uparrow_B, \downarrow_D)/S_{0,2}$ anticrossing for readout, we perform a similar sequence but starting deep in the (0,2) region where the ground states is $S_{0,2}$. Via diabatic pulsing through the $T^-/S_{0,2}$ anticrossing (outside the detuning range of panel f), we prepare the system in the excited $S_{0,2}$ near zero detuning to then ramp to the readout point. We observe a similar resonator ring-up followed by a decay with now a $T_1 \sim 270 \pm 50$ ns. We plot the data and the control in Fig. 5i. By measuring the decay constant as a function of detuning near the readout points, we find that T_1 ranges between 100-200 ns (200-400 ns) in the low (high) magnetic field case, with larger values reported further from the readout point. We hypothesize that the difference in T_1 for the two cases is related to the state decay happening primarily between the $T_{0,2}$ and $S_{0,2}$ at low fields - a spin decay within the QD - while at high magnetic fields the decay occurs between the $(\uparrow_B, \downarrow_D)$ and $(\downarrow_B, \downarrow_D)$ states - a decay within the Boron atom.

Overall, our results show that, in spin systems with lifted SB due to orbital states, the spin state can be read selectively and positively by making use of the different detuning points at which the dispersive signal of the $(\uparrow_B, \downarrow_D)$ and $T_{1,1}^-$ measurement outcomes manifest. While SOC is present in our system, resulting in a finite Δ_{sf} and g -factor difference, neither are required for readout using orbital states, allowing the readout mechanism to be extended to systems lacking strong SOC such as electrons in silicon. In such systems ($\Delta_{sf} = 0$, $g_D = g_B$), the two readout points correspond to a Singlet or Triplet (T^\pm , T^0) outcome. We discuss this further in App. D 2.

V. CONCLUSION

We have presented a novel spin readout methodology based on the detuning-dependent polarizability of the two-spin system in a semiconductor DQD to perform positive spin readout even when SB lifting mechanisms are present. We demonstrate this readout mechanism in two situations: Readout in the presence of SOC leading to spin flip tunnel coupling between the T^- and $S_{2,0}$ states, and spin-blockade lifting due to the presence of excited orbital states.

Our work and methodology opens new opportunities to (i) study the fundamentals of SB, its angular dependence in SOC systems and its impact on the ultimate readout fidelity, (ii) utilize the selective and positive nature of the readout to enhance the spin readout fidelity, detect state leakage and facilitate quantum tomography and (iii) explore the hybrid QD-acceptor and its interaction with a microwave resonator as a system for quantum information processing.

METHODOLOGY

Fabrication details. The transistors used in this study consists of a single gate silicon-on-insulator (SOI) nanowire transistor with a channel width of 120 nm, a length of 60 nm and height of 8 nm on top of a 145-nm-thick buried oxide. The silicon layer has a Boron doping density of $5 \cdot 10^{17} \text{ cm}^{-3}$. The silicon layer was patterned to create the channel using optical lithography, followed by a resist trimming process. The transistor gate stack consists of 1.9 nm HfSiON - leading to a total equivalent oxide thickness of 1.3 nm - capped by 5 nm TiN and 50 nm polycrystalline silicon. After gate etching, a Si_3N_4 layer (10 nm) was deposited and etched to form a first spacer on the sidewalls of the gate, then 18-nm-thick Si raised source and drain contacts were selectively grown before source/drain extension implantation and activation annealing. A second spacer was formed, followed by source/drain implantations, an activation spike anneal and salicidation (NiPtSi). The nanowire transistor and superconducting resonator were connected via Al/Si 1% bond wires.

Measurement set-up. Measurements were performed at the base temperature of a dilution refrigerator ($T \sim 10$ mK). Low frequency signals (V_g , V_{bg}) were applied through Constantan twisted pairs and RC filtered at the MXC plate. Radio-frequency signals were applied through filtered and attenuated coaxial lines to a coupling capacitor at the input of the LC resonator. Fast pulsing signals were applied through attenuated coaxial CuNi lines to an on-PCB (printed circuit-board) bias-T connected to the source of the transistor. The resonator (characteristic frequency 2.1 GHz) consists of a NbTiN superconducting spiral inductor ($L \sim 30$ nH), coupling capacitor ($C_c \sim 40$ fF) and low-pass filter fabricated by *Star Cryoelectronics*. For exact details of the super-

conducting chiplet see ref. [42]. The PCB was made from 0.8-mm-thick RO4003C with an immersion silver finish. The reflected rf signal was amplified at 4 K and room temperature, followed by quadrature demodulation (Polyphase Microwave AD0540B), from which the amplitude and phase of the reflected signal were obtained (homodyne detection).

Readout pulse sequence. The data in Fig. 3d consists of 100,000 shots at each detuning point, resulting in an average resonator response of the initialised states. After the readout measurement cycle in Fig. 3c, we wait for 100 microseconds in the (1,1) region to ensure the spin in the QD has decayed to the \downarrow ground state. This ensures only the $(\uparrow_B, \downarrow_D)$ and $(\downarrow_B, \downarrow_D)$ states can be initialised. For the time domain data (Fig. 3d-f), the time constant of the resonator ring up ($\tau \sim 80$ ns) is in good agreement with the bandwidth of our resonator ($\kappa/2\pi \sim 3$ -4 MHz with the exact value depending on magnetic field, and $\tau = 2/\kappa$). For readout at R_A , we estimate the state decay constant T_1 from the exponential decay of the signal after the initial rise. For readout at R_P , the initialised signal rises more slowly ($\tau \sim 95$ ns) as compared to the control ($\tau \sim 80$ ns).

Fit of time traces to extract T_1 at the readout point. To extract the state decay constants from the time-traces in Fig. 3 e and Fig. 5h and i, we fit the data with a model combining the ring-up of the resonator (determined by $\tau \sim 80$ ns) with capacitive signal contributions arising from the ground (C_{gnd}) and excited state (C_{exc}) where the excited state exponentially decays into the ground determined by a time constant T_1 :

$$C_{\text{total}} = \left(1 - e^{-\frac{t}{\tau}}\right) \left[C_{\text{exc}} e^{-\frac{t}{T_1}} + C_{\text{gnd}} \left(1 - e^{-\frac{t}{T_1}}\right) \right] \quad (1)$$

where t is the measurement time. We use a least square fit to extract T_1 and estimate the uncertainty from the covariance of the fit.

ACKNOWLEDGEMENT

This research was supported by the UK's Engineering and Physical Sciences Research Council (EPSRC) via the Cambridge NanoDTC (EP/L015978/1). F.E.v.H. acknowledges funding from the Gates Cambridge fellowship (Grant No. OPP1144). J. W. A. R. acknowledges funding from the EPSRC Core-to-Core International Network Grant "Oxide Superspin" (No. EP/ P026311/1). M.F.G.Z. acknowledges a UKRI Future Leaders Fellowship [MR/V023284/1]. L.P. acknowledges support from The Winton Programme for the Physics of Sustainability. MB acknowledges funding from the Emmy Noether Programme of the German Research Foundation (DFG) under grant no. BE 7683/1-1.

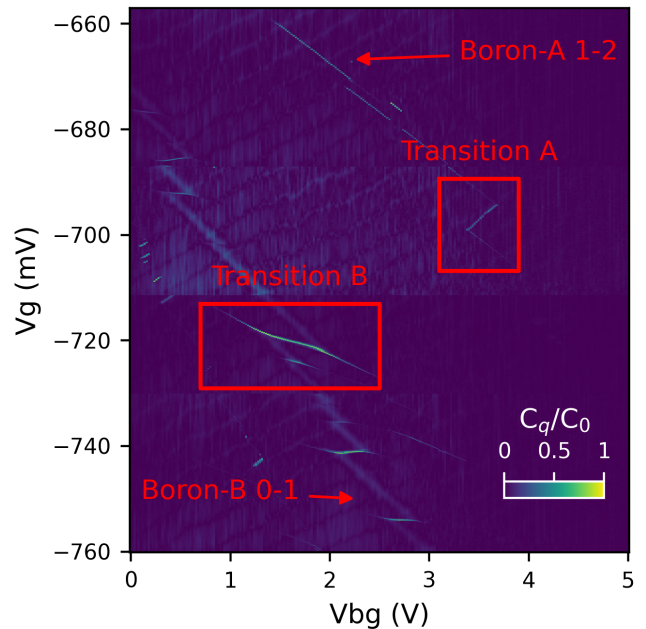


FIG. 6. Stability map showing the relative location of ICT A and B.

Appendix A: Stability map showing transitions A and B

The stability map of the device under study shows two Boron-reservoir transitions (red arrows) intersected by several Boron-quantum-dot-transitions. The different Boron acceptors and QDs can be distinguished by their different slope with respect to V_{bg} and V_{g} indicating different gate lever arms α . The charge occupation of the Boron atoms was deduced from the magneto-spectroscopy. Since Boron atoms can hold at most two holes, and the Boron involved in ICT A already contains two, we conclude that the Boron atoms involved in ICT A and B are distinct Boron atoms. This is supported by the difference in slope (different α) and tunnel rate of the two Boron-reservoir transitions.

Appendix B: Modelling Energy levels and Magneto-spectroscopy

We introduce the following Hamiltonian to simulate the energy level diagrams and magneto-spectroscopy in this work. We consider first two charge islands with occupation (N_L, N_R) occupied by a total of two spins. In the following, we assume the left dot is singly/not occupied, while the right dot is singly/doubly occupied. In the presence of SOC, it is easier to describe the (1,1) occupation in the single spins basis ($|\uparrow_l, \uparrow_r\rangle$, $|\downarrow_l, \uparrow_r\rangle$, $|\uparrow_l, \downarrow_r\rangle$, and $|\downarrow_l, \downarrow_r\rangle$). In the (0,2) occupation, we only include the singlet $|S_{0,2}\rangle$ [50]. In this basis, the Hamilto-

nian of the system can be found in Eq. (B1), which is a generalization of Ref. [18, 50]. The Zeeman energies are determined by the two g factors g_l and g_r for the two QDs respectively, while the (1,1) region is connected to

$$H = \frac{1}{2} \begin{bmatrix} \varepsilon + (g_l + g_r)B & 0 & 0 & 0 & -\Delta_{\text{sf}} \\ 0 & \varepsilon + (-g_l + g_r)B & 0 & 0 & -\Delta_{\text{sc}} \\ 0 & 0 & \varepsilon + (g_l - g_r)B & 0 & \Delta_{\text{sc}} \\ 0 & 0 & 0 & \varepsilon + (-g_l - g_r)B & \Delta_{\text{sf}} \\ -\Delta_{\text{sf}} & -\Delta_{\text{sc}} & \Delta_{\text{sc}} & \Delta_{\text{sf}} & -\varepsilon \end{bmatrix} \quad (\text{B1})$$

This Hamiltonian allows us to calculate the energy level diagrams shown in this paper. To simulate the magneto-spectroscopy, we extract the capacitive signal of the ground state arising from the cyclical variations in charge occupations driven by the tone of the resonator. This gives rise to a parametric capacitance (quantum and tunneling capacitance [46]). We neglect contributions by relaxation events giving rise to Sisyphus resistance [54]. The signal arises whenever two states anticross as this allows the resonator to drive differences in the charge occupation of the QDs. For a two level system with tunnel coupling Δ_0 in the slow relaxation limit (negligible tunneling capacitance), this results in a capacitance of:

$$C_p = \frac{(\epsilon\alpha)^2}{2} \frac{\Delta_0^2}{[(\epsilon - \epsilon_0)^2 + \Delta_0^2]^{3/2}} \chi_c \quad (\text{B2})$$

where C_p is the parametric capacitance, α the lever arm, ϵ_0 the location of the anticrossing in detuning, and χ_c the charge polarisation. It is worth noting that a smaller Δ_0 will result in sharper and brighter transitions (as long as $\Delta_0 > f_r$ [54, 55]). In the limits described, an intuitive understanding of the capacitance signal arising from a given energy level diagram can be gained from the second derivative (i.e. the curvature) of the energy level with detuning arising from the anticrossing of two states [56].

At zero magnetic field, the spin anti-parallel to $S_{0,2}$ anticrossing dominates the ground state of the system and therefore provides the source of the capacitive signal. Once a magnetic field is applied, the $T_{1,1}^-$ state is lowered below the (\uparrow, \downarrow) and (\downarrow, \uparrow) states which for $g_r - g_l \ll \bar{g}$ and $\Delta_{\text{sf}} \ll \Delta_{\text{sc}}$ can be found analytically as $\varepsilon \gtrsim [\Delta_{\text{sc}}^2 - (2\bar{g}\mu_B B)^2] / (4\bar{g}\mu_B B)$, otherwise the solution can be found numerically. Once $2\bar{g}\mu_B B \gtrsim \Delta_{\text{sc}}$ this results in the $T_{1,1}^-$ cutting off the anti-parallel to $S_{0,2}$ signal at zero detuning. If $\Delta_{\text{sf}} > 0$, the $T_{1,1}^-$ will then anticross with the $S_{0,2}$ giving rise to a new capacitive signal whose centre follows the hyperbolic expression above.

In the presence of an orbital (or valley) excited state in the right dot (Section IV), separated from the ground state in the right by an energy δ_o , we can extend the model in Eq. (B1) to include the state $|T_{0,2}^- \rangle$. Once

the $|S_{0,2} \rangle$ via a spin-conserving (Δ_{sc}) and a spin-flip (Δ_{sf}) tunnel couplings [51], the latter arising from the presence of SOC and thus potentially different spin quantization axes between the left and right QDs [52, 53].

$2g_r\mu_B B \gtrsim \delta_o$, the $T_{0,2}^-$ is also lowered below the $S_{0,2}$ state. At this point, the ground state anticrossing switches from the $T_{1,1}^-/S_{0,2}$ to the $T_{1,1}^-/T_{0,2}^-$ at $\varepsilon = \delta_o + 1/2 (g_l - g_r)\mu_B B$. For the sake of simplicity of the model, we assume that the overlap of the two states with the left QD are similar enough not to meaningfully alter the tunnel coupling, or the g -factor. Therefore, we assume Δ_{sc} and Δ_{sf} to be the same for both $|S_{0,2} \rangle$ and $|T_{0,2}^- \rangle$, as confirmed by the experimental measurement in Section IV.

Appendix C: Reduction in readout fidelity of projective measurements due to imperfect adiabatic transfer

In spin measurements making use of projective SB, any size anticrossing between the \downarrow, \downarrow and $S_{2,0}$ states will introduce errors in the readout fidelity to distinguish between the parallel and anti-parallel spin configurations. Take as an example an experiment in which we aim to distinguish between the (\downarrow, \downarrow) and (\uparrow, \downarrow) . To measure these spin states the DQD is pulsed into the (2,0) charge occupation. In the absence of Δ_{sf} , this leads to the projection of the (\uparrow, \downarrow) into $S_{2,0}$, while the (\downarrow, \downarrow) remains unchanged.

In systems experiencing SOC such that $\Delta_{\text{sf}} > 0$, this projection requires a diabatic state transfer across the $(\downarrow, \downarrow)/S_{2,0}$ anticrossing. For any energy pulsing rate ν and anticrossing Δ_{sf} , the probability of a diabatic transition is given by the Landau-Zener single passage probability [57]:

$$P_{LZ} = \exp\left(-2\pi \frac{\Delta_{\text{sf}}^2}{\hbar\nu}\right). \quad (\text{C1})$$

An imperfect diabatic transition across the anticrossing will limit the maximum state fidelity achievable via projective SB but, since the direct-dispersive method in this work does not require diabatic state transfer, it does not limit the fidelity of direct-dispersive methods. We note that this limit in fidelity is not arising from the signal-to-noise ratio, but rather from a projection error and therefore cannot be enhanced by higher quality readout circuitry.

To illustrate the severity of this problem, take the system discussed in Sections 2 and 3 of this work, where $\Delta_{\text{sf}} = 3.4 \text{ GHz} = 14 \mu\text{eV}$. To achieve a state transfer fidelity of 99 % this requires a pulse rate of 29.6 MeV/s. While this figure is already quite sizable (realistic pulse rates likely range on the order of 0.1-30 MeV/s depending on electrical equipment, filtering and device architecture), for every additional 9 of fidelity, the pulse rate has to increase by a factor of 10. This idea can be extended even to systems where SOC is weak (such as electrons in Si). Any small SOC will result in a Δ_{sf} , ultimately limiting the maximum achievable fidelity of any projective SB method.

Appendix D: Readout locations for hole and electron systems

In this section, we will discuss how different anticrossings can be used for state readout and the impact of magnetic field on the anticrossing separation of these states. For the purposes of clarity, we will split this section into two regimes: (i) Systems with strong SOC (e.g. hole spins in Si, Ge), resulting in significant Δ_{sf} but where we neglect low-lying orbital states, and (ii) systems with weak SOC (e.g. electrons spins in Si), where $\Delta_{\text{sf}} = 0$ and $g_l = g_r$ but low-lying orbital states are taken into account. Holes in QDs can exhibit both SOC and low lying orbital states (not discussed here) leading to a combination of the two effects.

1. Readout in systems with strong SOC

To discuss the readout points available for systems with strong SOC, we plot a simulated magneto-spectroscopy map, energy level diagrams, and quantum capacitance signals for a DQD system with $\Delta_{\text{sc}} = 10 \text{ GHz}$, $\Delta_{\text{sf}} = \Delta_{\text{sc}}/4$, and $g_l = 1.5$, $g_r = 2.5$ (Fig. 7). In this case, we do not consider orbital excited states.

At elevated magnetic fields, the $T_{1,1}^-$, $(\uparrow\downarrow)$, $(\downarrow\uparrow)$ and $T_{1,1}^+$ each anticross with the $S_{2,0}$ giving rise to four distinct readout points which can be used to perform full state tomography. Given a long enough T_1 , combined with slow enough ramp rates to ensure adiabatic passage of the anticrossings, the distinct readout points could allow a full characterisation of the state of the two spin system in a complementary way to what has been demonstrated in ref [58]. The ability to subsequently measure the occupation of the states may be used to detect state leakage out of the computational subspace.

To allow for sufficient visibility between the states, the readout locations need to be separated from each other to avoid signal overlap, as was discussed in App. F. This can be done either by changing the tunnel coupling, as discussed before, or by increasing the magnetic field: The T^+/S and T^-/S each move in detuning with magnetic field described by $\varepsilon_{\pm} = \pm [\Delta_c^2 - (2\bar{g}\mu_B B)^2] / 4\bar{g}\mu_B B$ (see

red and pink dashed lines in Fig. 7a). For the anti-aligned states, the separation is determined by the difference in g-factor $\delta g = g_r - g_l$ giving $\varepsilon_{(\uparrow,\downarrow)/(\downarrow,\uparrow)} \approx \pm \delta g \mu_B B / 2$ (white dashed lines).

2. Readout in systems with orbital excited states

Low-lying orbital (or valley) states are common in gate-defined QDs and such their effect on the readout positions should be considered. While, it was more appropriate to describe the case of holes in Si in the single spin basis due to their sizable g-factor difference, for electron in Si, where g-factors tend to be isotropic and SOC is weak, it is more practical to use the Singlet-Triplet basis. We define the singlet and unpolarized triplet as $S_{1,1} = (\downarrow, \uparrow - \uparrow, \downarrow) / \sqrt{2}$ and $T_{1,1}^0 = (\downarrow, \uparrow + \uparrow, \downarrow) / \sqrt{2}$, respectively. To provide a complete discussion, we additionally include the three Triplet states in the (0,2) charge occupancy involving the orbital excited state.

We plot a simulated magneto-spectroscopy map, energy level diagrams and quantum capacitance signals for a DQD housing two spins with $\Delta_c = 10 \text{ GHz}$, $\delta_o = 4\Delta_c$ and $g_l, g_r = 2$ ($\Delta_{\text{sf}} = 0$) in Fig. 8. The existence of the orbitally excited $T_{0,2}$ states significantly increases the complexity of the energy level diagrams (Fig. 7c,d,e). However, the quantum capacitance only arises from a few anticrossings: $S_{1,1}/S_{0,2}$, $T_{1,1}^-/T_{0,2}^-$, $T_{1,1}^0/T_{0,2}^0$, $T_{1,1}^+/T_{0,2}^+$, which are marked in blue/green, red/magenta, black/cyan and pink/orange respectively. In principle the three T/T anticrossings shift in magnetic field according to their g-factor difference ($g_l - g_r$) but since we have set all g-factors to be the same (as is typical for electron in Si) this does not occur here. As a result, only two distinct readout locations are present arising from the S/S anticrossing at $\varepsilon = 0$ and from the three T/T anticrossings located at $\varepsilon = \delta_o$ (Fig. 8c,d,e). These readout points are present at all magnetic fields, allowing for singlet-triplet readout independent of the magnetic field intensity.

To increase readout visibility, we again aim to improve the separation of the readout locations. These are fixed with magnetic field in this case. We therefore require the orbital (or valley) energy δ_o to be sufficiently large compared to the tunnel coupling Δ_c . This can be done by either careful engineering of the QDs to result in larger δ_o or by reducing Δ_c via the use of tunnel barrier gates. We note, the methodology described here can also be extended to other QD systems such as readout of spin-charge hybrid qubits [59, 60] where the two states of the computational basis experience distinct anticrossings separated from each other in detuning.

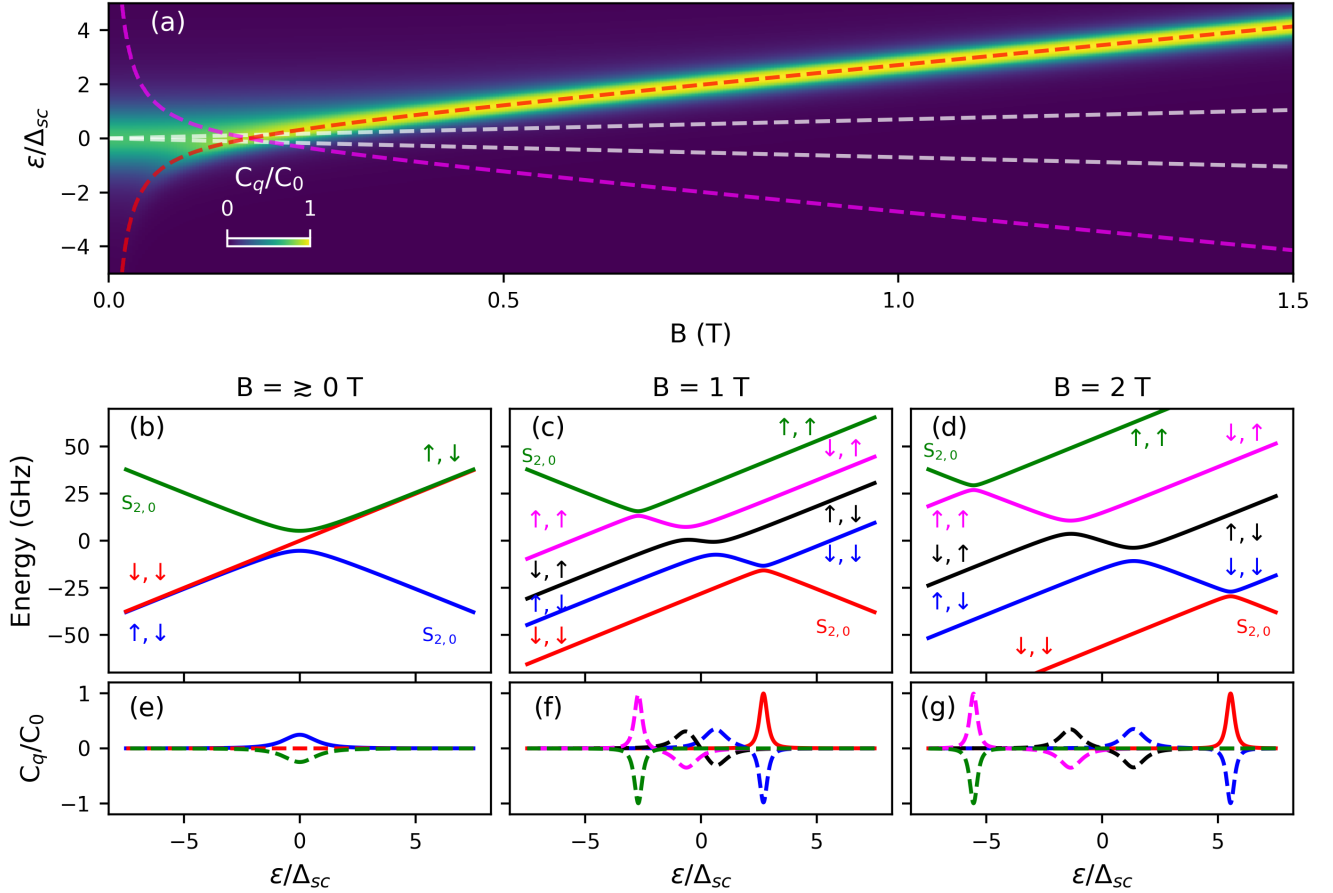


FIG. 7. Readout locations for systems with strong SOC: a) Simulated magneto-spectroscopy of a two spin system with $\Delta_{sf} = 10$ GHz, $\Delta_{sf} = \Delta_{sf}/4$, and $g_l = 1.5, g_r = 2.5$. The location of the $T_{1,1}^-/S_{2,0}$, $T_{1,1}^+/S_{2,0}$ anticrossings are marked with dashed lines in red and pink while those for the $(\uparrow, \downarrow)/S_{2,0}$ and $(\downarrow, \uparrow)/S_{2,0}$ are marked in white. b,c,d) Energy level diagrams at $B = 0, 1$ T and 2 T with d,e,f) the quantum capacitance arising from each state states. At elevated magnetic field there are four readout points corresponding to the $T_{1,1}^-$, (\uparrow, \downarrow) , (\downarrow, \uparrow) and $T_{1,1}^+$ states.

Appendix E: T^-/S anticrossing detuning dependence with Magnetic field

To further characterise the behaviour of the readout in the T^-/S coupled regime of ICT A, we characterise the location of the excited $(\uparrow_B, \downarrow_D)/S$ anticrossing as a function of magnetic field. We carry out readout experiments like those described in section II and measure the separation of the ground state signal arising from the T^-/S anticrossing from the excited state signal arising from the $(\uparrow_B, \downarrow_D)/S$ anticrossing (Fig. 9a-c). We find this dependency to be approximately linear, with a slope given by $\Delta\varepsilon = \hat{g}\mu_B B$ from which we extract \bar{g} of $2.01 \pm .08$, in line with what was extracted from magneto-spectroscopy (Fig. 9d,e).

Appendix F: Effect of anticrossing separation on readout visibility

The readout mechanism described in this paper makes use of the dispersive signal generated by various anticrossings to distinguish between spin states. When two such anticrossings are not sufficiently separated, signal from both states can be picked up at the readout point, reducing the discriminating visibility.

To demonstrate this concept, we plot the capacitive signal of two anticrossings with tunnel coupling $\Delta_0 = \Delta_e = \Delta_g$, and separated by $\varepsilon_{g(e)} = \pm\varepsilon_0/2$ (Fig. 10a), representing a ground and excited state readout outcome. Additionally, we plot the difference in signal (in red) of the two states, showing the discriminating amplitude of the two readout outcomes. Note that if we wanted to distinguish these two states, there would be a loss of visibility due to the overlap between the signals. We define the visibility as the difference in capacitive signal aris-

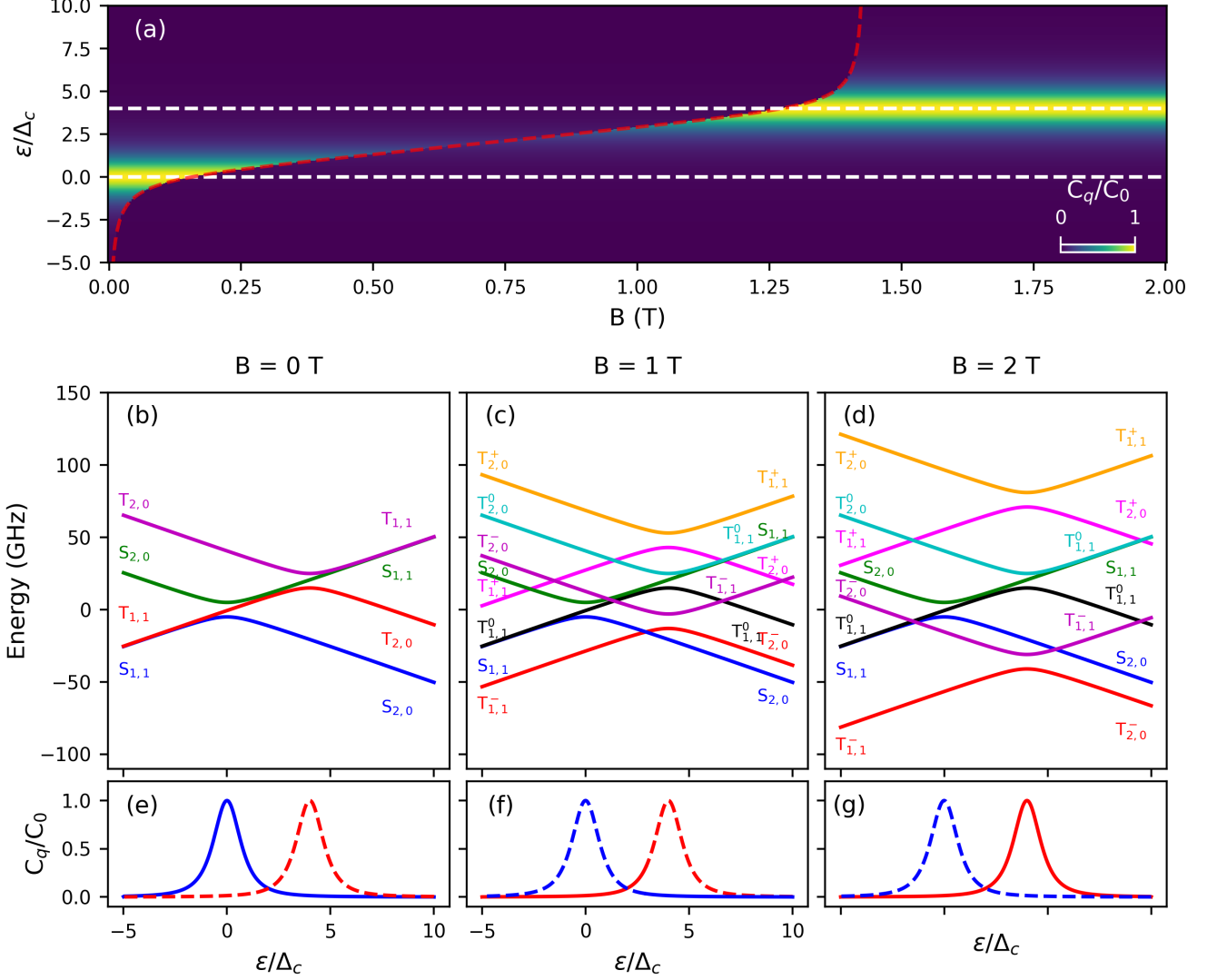


FIG. 8. Readout locations for systems with orbital excited states: a) Simulated magneto-spectroscopy of a electron double quantum dot with $\Delta_c = 10$ GHz, $\delta_o = 4\Delta_c$ and $g_l, g_r = 2$ ($\Delta_{sf} = 0$). The location of the S/S (left), and T/T (right) anticrossings are marked with white dashed lines, the location of the T⁻/S crossing is marked with a red dashed line. b,c,d) Energy level diagrams at $B = 0, 1$ T and 2 T with e,f,g) the quantum capacitance arising of the $S_{1,1}$ and $T_{1,1}$ states. In each case the capacitance arising from the instantaneous ground state is plotted in a solid line, while excited states are plotted in dashed lines. There are two readout points corresponding to the $S_{1,1}$ and $T_{1,1}$ outcomes.

ing from the two anticrossings. Under the approximation that, in the vicinity of each anticrossing, the energy spectrum can be seen just as a two level system, we use Eq. B2 to find:

$$\Delta C_p \approx \frac{(e\alpha)^2}{2} \left[\frac{\Delta_e^2}{[(\varepsilon - \varepsilon_e)^2 - \Delta_e^2]^{1.5}} P_e - \frac{\Delta_g^2}{[(\varepsilon - \varepsilon_g)^2 - \Delta_g^2]^{1.5}} P_g \right], \quad (\text{F1})$$

where we have included a time dependent state prob-

ability $1 - P_g = P_e = e^{-t/T_1}$, and $\varepsilon_{g(e)}$ are the magnetic field dependent detuning locations of the ground (excited). This equation can be used to describe the capacitive signal in Fig. 3d.

Note that in Fig. 10a both the maximum discriminating signal amplitude ($|C_p|/C_0$), and the detuning location at which it occurs (ε_{max} , red dashed lines) differ from that of the pure signal (blue and orange dashed lines). We now analyse the difference by simulating the maximum discriminating signal amplitude (Fig. 10b) and detuning location (compared to the maxima of the pure signal amplitudes, Fig. 10c) as a function of the reduced state separation, ε_0/Δ_0 . We find that the discriminating

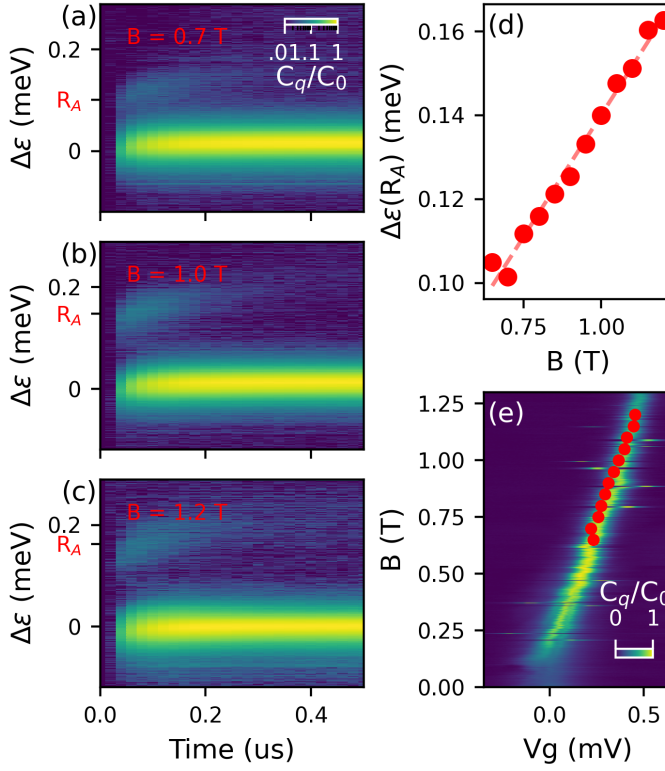


FIG. 9. Characterisation of Readout point location for spin-orbit lifted readout against magnetic field: (a-c) Capacitive signal vs readout time like that in Fig. 3d at three different fields. Note that the short-lived excited state signal (marked with R_A) shifts with respect to the long-lived ground state signal. (d) Center of excited state signal location relative to the ground state signal as a function magnetic field. The dashed line has a slope of $\partial\epsilon/\partial B = \bar{g}\mu_B$ with \bar{g} of $2.01 \pm .08$. (e) The line in d overlaid on the magneto-spectroscopy data shown in Fig. 2d showing a good match.

signal rises steeply around $\epsilon_0 = \Delta_0$ and plateaus at the signal amplitude of the pure anticrossings. When ϵ_0/Δ_0 is small, the optimum detuning readout point is separated by Δ_0 rather than ϵ_0 , i.e. the optimum readout points are pushed outwards. These points shift towards their expected $\epsilon_0/2$ positions as ϵ_0 is increased beyond Δ_0 .

From these considerations, we can draw the following conclusions: (i) For low level separation $\epsilon_0/\Delta_0 \ll 1$ the readout points needs to be carefully selected to improve visibility. (ii) The most significant gain in visibility occurs around $\epsilon_0 = \Delta_0$ but increasing ϵ_0 to beyond a few Δ_0 does not lead to significant signal improvements (e.g. a ϵ_0/Δ_0 of 5 will give $> 99\%$ visibility). Note that in the cases of asymmetric coupling of the two states (i.e. $\Delta_e \neq \Delta_g$), the relevant metric is $\epsilon_0/\Delta_g(\epsilon_0/\Delta_e)$ for mea-

suring the excited (ground) state, i.e. the ground and excited states should be separated by significantly more than the Δ of any other anticrossings not directly measured.

To improve ϵ_0/Δ_0 , two general approaches can be

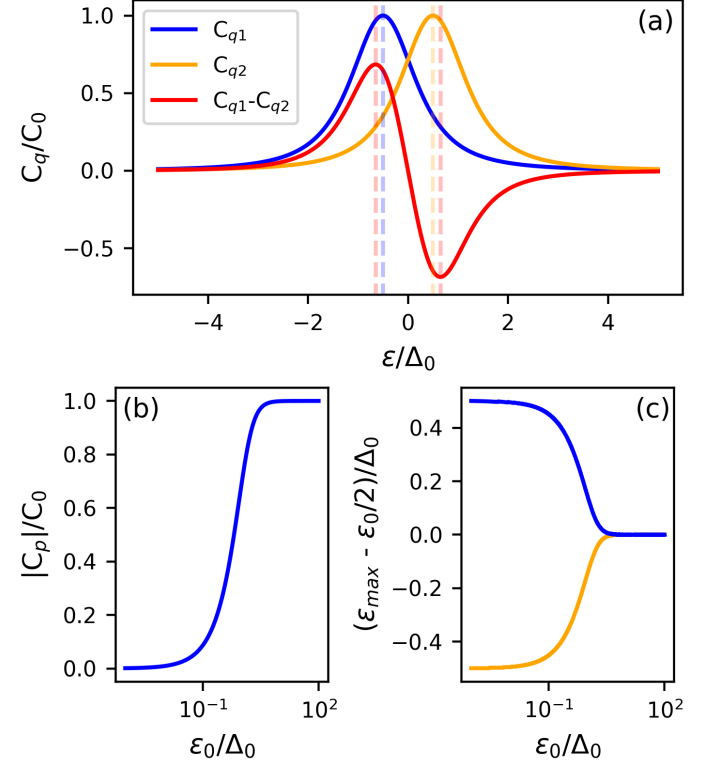


FIG. 10. Effect of anticrossing separation on readout visibility: (a) Signal from two states (blue, orange) separated in detuning by $\epsilon_0 = \Delta_0$ and difference in the signal (red). The maxima (minima) of the states and their differences are marked with dashed lines. Note that both the maximum amplitude as well as the readout points of maximum signal differ between the difference and pure signal amplitudes. (b) Effect of state separation ϵ_0 on maximum differentiable signal, corresponding to the peak value of the red curve in a as ϵ_0 is increased. The strongest gain occurs around $\epsilon_0 = \Delta_0$. (c) Shift of the optimum readout point from its pure signal maximum given by the two extremes of the red curve in (a) with respect to ϵ_0 . As the separation is increased the optimum readout points approach that of the pure signal amplitudes.

taken: (i) The magnetic field can be adjusted to maximise the separation ϵ_0 , or to select an anticrossing with low Δ as the anticrossing not to be measured. (ii) Tunnel barriers (if present) can be used to directly decrease Δ in the readout phase. The former approach will be addressed in App. D. With the latter approach, care should be taken not to reduce the Δ of the state to be measured below the resonator frequency f_r when utilising gate dispersive readout as this reduces the signal amplitude [55].

- [1] A. Bienfait, J. J. Pla, Y. Kubo, M. Stern, X. Zhou, C. C. Lo, C. D. Weis, T. Schenkel, M. L. W. Thewalt, D. Vion, D. Esteve, B. Julsgaard, K. Mølmer, J. J. L. Morton, and P. Bertet, Reaching the quantum limit of sensitivity in electron spin resonance, *Nat. Nanotechnol.* **11**, 253 (2016).
- [2] V. Ranjan, S. Probst, B. Albanese, T. Schenkel, D. Vion, D. Esteve, J. J. L. Morton, and P. Bertet, Electron spin resonance spectroscopy with femtoliter detection volume, *Appl. Phys. Lett.* **116**, 184002 (2020).
- [3] R. P. Budoyo, K. Kakuyanagi, H. Toida, Y. Matsuzaki, and S. Saito, Electron spin resonance with up to 20 spin sensitivity measured using a superconducting flux qubit, *Appl. Phys. Lett.* **116**, 194001 (2020).
- [4] R. J. Schoelkopf, P. Wahlgren, A. A. Kozhevnikov, P. Delsing, and D. E. Prober, The radio-frequency single-electron transistor (RF-SET): A fast and ultrasensitive electrometer, *Science* **280**, 1238 (1998).
- [5] A. Aassime, G. Johansson, G. Wendin, R. J. Schoelkopf, and P. Delsing, Radio-frequency single-electron transistor as readout device for qubits: Charge sensitivity and backaction, *Phys. Rev. Lett.* **86**, 3376 (2001).
- [6] S. Schaal, I. Ahmed, J. A. Haigh, L. Hutin, B. Bertrand, S. Barraud, M. Vinet, C.-M. Lee, N. Stelmashenko, J. W. A. Robinson, J. Y. Qiu, S. Hacoen-Gourgy, I. Siddiqi, M. F. Gonzalez-Zalba, and J. J. L. Morton, Fast gate-based readout of silicon quantum dots using josephson parametric amplification, *Phys. Rev. Lett.* **124**, 067701 (2020).
- [7] J. M. Elzerman, R. Hanson, L. H. W. van Bevern, B. Witkamp, L. M. K. Vandersypen, and L. P. Kouwenhoven, Single-shot read-out of an individual electron spin in a quantum dot, *Nature* **430**, 431 (2004).
- [8] K. Ono, D. Austing, Y. Tokura, and S. Tarucha, Current rectification by pauli exclusion in a weakly coupled double quantum dot system, *Science* **297**, 1313 (2002).
- [9] D. Keith, M. G. House, M. B. Donnelly, T. F. Watson, B. Weber, and M. Y. Simmons, Single-shot spin readout in semiconductors near the shot-noise sensitivity limit, *Phys. Rev. X* **9**, 41003 (2019).
- [10] F. Borjans, X. Mi, and J. Petta, Spin digitizer for high-fidelity readout of a cavity-coupled silicon triple quantum dot, *Phys. Rev. App.* **15**, 044052 (2021).
- [11] J. Z. Blumoff, A. S. Pan, T. E. Keating, R. W. Andrews, D. W. Barnes, T. L. Brecht, E. T. Croke, L. E. Euliss, J. A. Fast, C. A. Jackson, A. M. Jones, J. Kerckhoff, R. K. Lanza, K. Raach, B. J. Thomas, R. Velunta, A. J. Weinstein, T. D. Ladd, K. Eng, M. G. Borselli, A. T. Hunter, and M. T. Rakher, Fast and high-fidelity state preparation and measurement in triple-quantum-dot spin qubits, *PRX Quantum* **3**, 010352 (2022).
- [12] G. A. Oakes, V. N. Ciriano-Tejel, D. F. Wise, M. A. Fogarty, T. Lundberg, C. Lainé, S. Schaal, F. Martins, D. J. Ibberson, L. Hutin, B. Bertrand, N. Stelmashenko, J. W. A. Robinson, L. Ibberson, A. Hashim, I. Siddiqi, A. Lee, M. Vinet, C. G. Smith, J. J. L. Morton, and M. F. Gonzalez-Zalba, Fast high-fidelity single-shot readout of spins in silicon using a single-electron box, *Phys. Rev. X* **13**, 011023 (2023).
- [13] R. Zhao, T. Tanttu, K. Y. Tan, B. Hensen, K. W. Chan, J. C. C. Hwang, R. C. C. Leon, C. H. Yang, W. Gilbert, F. E. Hudson, K. M. Itoh, A. A. Kiselev, T. D. Ladd, A. Morello, A. Laucht, and A. S. Dzurak, Single-spin qubits in isotopically enriched silicon at low magnetic field, *Nat. Commun.* **10**, 5500 (2019).
- [14] M. Urdampilleta, D. J. Niegemann, E. Chanrion, B. Jadot, C. Spence, P.-A. Mortemousque, C. Bäuerle, L. Hutin, B. Bertrand, S. Barraud, R. Maurand, M. Sanquer, X. Jehl, S. D. Franceschi, M. Vinet, and T. Meunier, Gate-based high fidelity spin readout in a CMOS device, *Nat. Nanotechnol.* **14**, 737 (2019).
- [15] D. J. Niegemann, V. El-Homsy, B. Jadot, M. Nurizzo, B. Cardoso-Paz, E. Chanrion, M. Dartiaillh, B. Klemt, V. Thiney, C. Bäuerle, P.-A. Mortemousque, B. Bertrand, H. Niebojewski, M. Vinet, F. Balestro, T. Meunier, and M. Urdampilleta, Parity and singlet-triplet high-fidelity readout in a silicon double quantum dot at 0.5 K, *PRX Quantum* **3**, 040335 (2022).
- [16] M. A. I. Johnson, M. T. Mkadzik, F. E. Hudson, K. M. Itoh, A. M. Jakob, D. N. Jamieson, A. Dzurak, and A. Morello, Beating the thermal limit of qubit initialization with a bayesian maxwell's demon, *Phys. Rev. X* **12**, 041008 (2022).
- [17] D. Keith, S. K. Gorman, L. Kranz, Y. He, J. G. Keizer, M. A. Broome, and M. Y. Simmons, Benchmarking high fidelity single-shot readout of semiconductor qubits, *New J. Phys.* **21**, 063011 (2019).
- [18] J. Danon and Y. V. Nazarov, Pauli spin blockade in the presence of strong spin-orbit coupling, *Phys. Rev. B* **80**, 041301 (2009).
- [19] S. Nadj-Perge, S. M. Frolov, J. W. W. van Tilburg, J. Danon, Y. V. Nazarov, R. Algra, E. P. A. M. Bakkers, and L. P. Kouwenhoven, Disentangling the effects of spin-orbit and hyperfine interactions on spin blockade, *Phys. Rev. B* **81**, 201305 (2010).
- [20] N. Shaji, C. B. Simmons, M. Thalakulam, L. J. Klein, H. Qin, H. Luo, D. E. Savage, M. G. Lagally, A. J. Rimberg, R. Joynt, M. Friesen, R. H. Blick, S. N. Copper-Smith, and M. A. Eriksson, Spin blockade and lifetime-enhanced transport in a few-electron Si/SiGe double quantum dot, *Nat. Phys.* **4**, 540 (2008).
- [21] A. C. Betz, R. Wacquez, M. Vinet, X. Jehl, A. L. Saraiva, M. Sanquer, A. J. Ferguson, and M. F. Gonzalez-Zalba, Dispersively detected pauli spin-blockade in a silicon nanowire field-effect transistor, *Nano Lett.* **15**, 4622 (2015).
- [22] D. Q. Wang, O. Klochan, J.-T. Hung, D. Culcer, I. Farrer, D. A. Ritchie, and A. R. Hamilton, Anisotropic pauli spin blockade of holes in a GaAs double quantum dot, *Nano Lett.* **16**, 7685 (2016).
- [23] V. F. Maisi, A. Hofmann, M. Rösli, J. Basset, C. Reichl, W. Wegscheider, T. Ihn, and K. Ensslin, Spin-orbit coupling at the level of a single electron, *Phys. Rev. Lett.* **116**, 136803 (2016).
- [24] T. Fujita, P. Stano, G. Allison, K. Morimoto, Y. Sato, M. Larsson, J.-H. Park, A. Ludwig, A. D. Wieck, A. Oiwa, and S. Tarucha, Signatures of hyperfine, spin-orbit, and decoherence effects in a pauli spin blockade, *Phys. Rev. Lett.* **117**, 206802 (2016).
- [25] J.-Y. Wang, G.-Y. Huang, S. Huang, J. Xue, D. Pan, J. Zhao, and H. Xu, Anisotropic pauli spin-blockade effect and spin-orbit interaction field in an InAs nanowire

- double quantum dot, *Nano Lett.* **18**, 4741 (2018).
- [26] H. Watzinger, J. Kukučka, L. Vukušić, F. Gao, T. Wang, F. Schäffler, J.-J. Zhang, and G. Katsaros, A germanium hole spin qubit, *Nat. Commun.* **9**, 3902 (2018).
- [27] D. Jirovec, A. Hofmann, A. Ballabio, P. M. Mutter, G. Tavani, M. Botifoll, A. Crippa, J. Kukučka, O. Sagi, F. Martins, J. Saez-Mollejo, I. Prieto, M. Borovkov, J. Arbiol, D. Chrastina, G. Isella, and G. Katsaros, A singlet-triplet hole spin qubit in planar Ge, *Nat. Mater.* **20**, 1106 (2021).
- [28] F. D. Palma, F. Oppliger, W. Jang, S. Bosco, M. Janík, S. Calcaterra, G. Katsaros, G. Isella, D. Loss, and P. Scarlino, Strong hole-photon coupling in planar Ge: probing the charge degree and wigner molecule states (2023), arXiv:2310.20661 [quant-ph].
- [29] F. Borsoi, N. W. Hendrickx, V. John, M. Meyer, S. Motz, F. van Riggelen, A. Sammak, S. L. de Snoo, G. Scappucci, and M. Veldhorst, Shared control of a 16 semiconductor quantum dot crossbar array, *Nat. Nanotechnol.* **19**, 21 (2024).
- [30] R. Li, F. E. Hudson, A. S. Dzurak, and A. R. Hamilton, Pauli spin blockade of heavy holes in a silicon double quantum dot, *Nano Lett.* **15**, 7314 (2015).
- [31] L. C. Camenzind, S. Geyer, A. Fuhrer, R. J. Warburton, D. M. Zumbühl, and A. V. Kuhlmann, A hole spin qubit in a fin field-effect transistor above 4 kelvin, *Nat. Electron.* **5**, 178 (2022).
- [32] R. Maurand, X. Jehl, D. Kotekar-Patil, A. Corna, H. Bohuslavskiy, R. Laviéville, L. Hutin, S. Barraud, M. Vinet, M. Sanquer, and S. De Franceschi, A CMOS silicon spin qubit, *Nat. Commun.* **7**, 13575 EP (2016).
- [33] F. N. M. Froning, L. C. Camenzind, O. A. H. van der Molen, A. Li, E. P. A. M. Bakkers, D. M. Zumbühl, and F. R. Braakman, Ultrafast hole spin qubit with gate-tunable spin-orbit switch functionality, *Nat. Nanotechnol.* **16**, 308 (2021).
- [34] N. Piot, B. Brun, V. Schmitt, S. Zihlmann, V. P. Michal, A. Apra, J. C. Abadillo-Uriel, X. Jehl, B. Bertrand, H. Niebojewski, L. Hutin, M. Vinet, M. Urdampilleta, T. Meunier, Y.-M. Niquet, R. Maurand, and S. D. Franceschi, A single hole spin with enhanced coherence in natural silicon, *Nat. Nanotechnol.* **17**, 1072 (2022).
- [35] J. Schuff, M. J. Carballido, M. Kotzagiannidis, J. C. Calvo, M. Caselli, J. Rawling, D. L. Craig, B. van Straaten, B. Severin, F. Fedele, S. Svab, P. C. Kwon, R. S. Eggli, T. Patlatiuk, N. Korda, D. Zumbühl, and N. Ares, Fully autonomous tuning of a spin qubit (2024), arXiv:2402.03931 [cond-mat.mes-hall].
- [36] M. J. Carballido, S. Svab, R. S. Eggli, T. Patlatiuk, P. C. Kwon, J. Schuff, R. M. Kaiser, L. C. Camenzind, A. Li, N. Ares, E. P. A. M. Bakkers, S. Bosco, J. C. Egues, D. Loss, and D. M. Zumbühl, A qubit with simultaneously maximized speed and coherence (2024), arXiv:2402.07313 [cond-mat.mes-hall].
- [37] N. W. Hendrickx, W. I. L. Lawrie, M. Russ, F. van Riggelen, S. L. de Snoo, R. N. Schouten, A. Sammak, G. Scappucci, and M. Veldhorst, A four-qubit germanium quantum processor, *Nature* **591**, 580 (2021).
- [38] X. Zhang, E. Morozova, M. Rimbach-Russ, D. Jirovec, T.-K. Hsiao, P. C. Fariña, C.-A. Wang, S. D. Oosterhout, A. Sammak, G. Scappucci, M. Veldhorst, and L. M. K. Vandersypen, Universal control of four singlet-triplet qubits (2023), arXiv:2312.16101 [cond-mat.mes-hall].
- [39] S. D. Liles, D. J. Halverson, Z. Wang, A. Shamim, R. S. Eggli, I. K. Jin, J. Hillier, K. Kumar, I. Vorreiter, M. Rendell, J. H. Huang, C. C. Escott, F. E. Hudson, W. H. Lim, D. Culcer, A. S. Dzurak, and A. R. Hamilton, A singlet-triplet hole-spin qubit in MOS silicon (2023), arXiv:2310.09722 [cond-mat.mes-hall].
- [40] F. Vigneau, F. Fedele, A. Chatterjee, D. Reilly, F. Kuemeth, M. F. Gonzalez-Zalba, E. Laird, and N. Ares, Probing quantum devices with radio-frequency reflectometry, *Appl. Phys. Rev.* **10**, 021305 (2023).
- [41] A. West, B. Hensen, A. Jouan, T. Tanttu, C.-H. Yang, A. Rossi, M. F. Gonzalez-Zalba, F. Hudson, A. Morello, D. J. Reilly, and A. S. Dzurak, Gate-based single-shot readout of spins in silicon, *Nat. Nanotechnol.* **14**, 437 (2019).
- [42] F.-E. von Horstig, D. J. Ibberson, G. A. Oakes, L. Cochrane, N. Stelmashenko, S. Barraud, J. A. W. Robinson, F. Martins, and M. F. Gonzalez-Zalba, Multimodule microwave assembly for fast read-out and charge noise characterization of silicon quantum dots (2023), arXiv:2304.13442 [cond-mat.mes-hall].
- [43] J. van der Heijden, T. Kobayashi, M. G. House, J. Salfi, S. Barraud, R. Laviéville, M. Y. Simmons, and S. Rogge, Readout and control of the spin-orbit states of two coupled acceptor atoms in a silicon transistor, *Sci. Adv.* **4**, eaat9199 (2018).
- [44] T. Lundberg, J. Li, L. Hutin, B. Bertrand, D. Ibberson, C.-M. Lee, D. Niegemann, M. Urdampilleta, N. Stelmashenko, T. Meunier, J. Robinson, L. Ibberson, M. Vinet, Y.-M. Niquet, and M. Gonzalez-Zalba, Spin quintet in a silicon double quantum dot: Spin blockade and relaxation, *Phys. Rev. X* **10**, 10.1103/PhysRevX.10.041010 (2020).
- [45] T. Lundberg, D. J. Ibberson, J. Li, L. Hutin, J. C. Abadillo-Uriel, M. Filippone, B. Bertrand, A. Nunenkamp, C.-M. Lee, N. Stelmashenko, J. W. A. Robinson, M. Vinet, L. Ibberson, Y.-M. Niquet, and M. F. Gonzalez-Zalba, Non-symmetric pauli spin blockade in a silicon double quantum dot, *npj Quantum Inf.* **10**, 1 (2024).
- [46] R. Mizuta, R. M. Otxoa, A. C. Betz, and M. F. Gonzalez-Zalba, Quantum and tunneling capacitance in charge and spin qubits, *Phys. Rev. B* **95**, 045414 (2017).
- [47] We define the g -factor at a particular magnetic field angle as $g = |g\vec{B}|/|\vec{B}|$ where g is the g -tensor.
- [48] A. E. Seedhouse, T. Tanttu, R. C. Leon, R. Zhao, K. Y. Tan, B. Hensen, F. E. Hudson, K. M. Itoh, J. Yoneda, C. H. Yang, A. Morello, A. Laucht, S. N. Coppersmith, A. Saraiva, and A. S. Dzurak, Pauli blockade in silicon quantum dots with spin-orbit control, *PRX Quantum* **2**, 010303 (2021).
- [49] A. J. Weinstein, M. D. Reed, A. M. Jones, R. W. Andrews, D. Barnes, J. Z. Blumoff, L. E. Euliss, K. Eng, B. H. Fong, S. D. Ha, D. R. Hulbert, C. A. C. Jackson, M. Jura, T. E. Keating, J. Kerckhoff, A. A. Kiselev, J. Matten, G. Sabbir, A. Smith, J. Wright, M. T. Rakher, T. D. Ladd, and M. G. Borselli, Universal logic with encoded spin qubits in silicon, *Nature* **615**, 817 (2023).
- [50] M. Veldhorst, C. H. Yang, J. C. C. Hwang, W. Huang, J. P. Dehollain, J. T. Muhonen, S. Simmons, A. Laucht, F. E. Hudson, K. M. Itoh, A. Morello, and A. S. Dzurak, A two-qubit logic gate in silicon, *Nature* **526**, 410 (2015).
- [51] C. X. Yu, S. Zihlmann, J. C. Abadillo-Uriel, V. P. Michal,

- N. Rambal, H. Niebojewski, T. Bedecarrats, M. Vinet, É. Dumur, M. Filippone, B. Bertrand, S. De Franceschi, Y.-M. Niquet, and R. Maurand, Strong coupling between a photon and a hole spin in silicon, *Nat. Nanotechnol.* **18**, 741 (2023).
- [52] A. Sen, G. Frank, B. Kolok, J. Danon, and A. Pályi, Classification and magic magnetic-field directions for spin-orbit-coupled double quantum dots (2023), arXiv:2307.02958.
- [53] van Riggelen-Doelman Floor, C.-A. Wang, S. L. Snoo, W. I. L. Lawrie, N. W. Hendrickx, M. Rimbach-Russ, A. Sammak, G. Scappucci, C. Déprez, and M. Veldhorst, Coherent spin qubit shuttling through germanium quantum dots (2023), arXiv:2308.02406.
- [54] M. Esterli, R. M. Otxoa, and M. F. Gonzalez-Zalba, Small-signal equivalent circuit for double quantum dots at low-frequencies, *Appl. Phys. Lett.* **114**, 253505 (2019).
- [55] L. Peri, M. Benito, C. J. B. Ford, and M. F. Gonzalez-Zalba, Unified linear response theory of quantum dot circuits (2023), arXiv:2310.17399 [cond-mat.mes-hall].
- [56] K. D. Petersson, C. G. Smith, D. Anderson, P. Atkinson, G. A. C. Jones, and D. A. Ritchie, Charge and spin state readout of a double quantum dot coupled to a resonator, *Nano Lett.* **10**, 2789 (2010).
- [57] S. Shevchenko, S. Ashhab, and F. Nori, Landau-Zener-Stückelberg interferometry, *Phys. Rep.* **492**, 1 (2010).
- [58] M. Nurizzo, B. Jadot, P.-A. Mortemousque, V. Thiney, E. Chanrion, D. Niegemann, M. Dartiailh, A. Ludwig, A. D. Wieck, C. Bäuerle, M. Urdampilleta, and T. Meunier, Complete readout of two-electron spin states in a double quantum dot, *PRX Quantum* **4**, 010329 (2023).
- [59] D. Kim, C. Simmons, D. Ward, J. Prance, T. S. Koh, J. King Gamble, D. Savage, M. Lagally, M. Friesen, S. Coppersmith, and M. Eriksson, Quantum control and process tomography of a semiconductor quantum dot hybrid, *Nature* **511**, 70 (2014).
- [60] W. Jang, M.-K. Cho, H. Jang, J. Kim, J. Park, G. Kim, B. Kang, H. Jung, V. Umansky, and D. Kim, Single-Shot Readout of a Driven Hybrid Qubit in a GaAs Double Quantum Dot, *Nano Lett.* **21**, 4999 (2021).